

An HI View of Galaxy Conformity: HI-rich Environment around HI-excess Galaxies

Jing Wang^{1*}, Paolo Serra¹, Gyula I. G. Józsa^{2,3,4}, Bärbel Koribalski¹,
 Thijs van der Hulst⁵, Peter Kamphuis¹, Cheng Li⁶, Jian Fu⁶, Ting Xiao⁶,
 Roderik Overzier⁷, Mark Wieringa¹, Enci Wang⁶

¹*Australia Telescope National Facility, CSIRO Astronomy and Space Science, PO box 76, Epping, NSW 1710, Australia*

²*SKA South Africa Radio Astronomy Research Group, 3rd Floor, The Park, Park Road, Pinelands, 7405, South Africa*

³*Rhodes University, Department of Physics and Electronics, Rhodes Centre for Radio Astronomy Techniques & Technologies, PO Box 94, Grahamstown, 6140, South Africa*

⁴*Argelander-Institut für Astronomie, Auf dem Hügel 71, D-53121 Bonn, Germany*

⁵*University of Groningen, Kapteyn Astronomical Institute, Landleven 12, 9747 AD, Groningen, The Netherlands*

⁶*Key Laboratory for Research in Galaxies and Cosmology, Shanghai Astronomical Observatory, Chinese Astronomical Society, 80 Nandan Rd, Shanghai 200030, China*

⁷*Observatório Nacional, Ministry of Science, Technology, and Innovation, Rio de Janeiro, Brazil*

Accepted 2014 ???? ?? Received 2014 ???? ??; in original form 2014 January

ABSTRACT

Using data taken as part of the Bluedisk project we study the connection between neutral hydrogen (HI) in the environment of spiral galaxies and that in the galaxies themselves. We measure the total HI mass present in the environment in a statistical way by studying the distribution of noise peaks in the HI data cubes obtained for 40 galaxies observed with WSRT. We find that galaxies whose HI mass fraction is high relative to standard scaling relations have an excess HI mass in the surrounding environment as well. Gas in the environment consists of gas clumps which are individually below the detection limit of our HI data. These clumps may be hosted by small satellite galaxies and/or be the high-density peaks of a more diffuse gas distribution in the inter-galactic medium. We interpret this result as an indication for a picture in which the HI-rich central galaxies accrete gas from an extended gas reservoir present in their environment.

Key words: galaxies:spiral; intergalactic medium

1 INTRODUCTION

Gas accretion is an important process in the evolution of galaxies. Galaxies like the Milky Way would run out of their gas in less than 1 Gyr given their current star formation rate unless their gas reservoir is continuously replenished (Kennicutt 1983). The source of this fresh gas is unknown but the majority is unlikely to be contained in gas-rich satellite galaxies because they can contribute at most 10 percent of the required gas mass (Kauffmann et al. 2010; Di Teodoro & Fraternali 2014,). Likewise, high-velocity HI clouds contribute 3-5 times less gas than required to sustain the Milky Way star formation (Richter 2012). A potentially more substantial source of fresh material is the cooling flow of low-

metallicity, ionised gas in a galaxy’s halo (Shull et al. 2009). This may be related to the “fountain” gas which is driven to a height of a few kpc from the disc by star formation, and may trigger a gas inflow rate very close to the star formation rate (Fraternali et al. 2013). Recent theoretical studies suggest that the fountain driven gas naturally produces an outside-in shrinking galactic disk (Elmegreen et al. 2014), which is consistent with what is observed for nearby dwarf galaxies (Zhang et al. 2012). However, it does not explain the observed inside-out growth of more massive disk galaxies (J. Wang et al. 2011), or their chemical evolution (Spitoni et al. 2013), which have been both explained in terms of a cosmological radial gas accretion (Kauffmann 1996, Spitoni et al. 2013).

In the framework of the standard Λ CDM cosmology, two modes of (radial) gas accretion occur. Gas entering the

* Email: j.wang@csiro.au

potential well of a galaxy gets shocked to the virial temperature of the dark matter halo at an early epoch of infall, and then gradually cools and falls onto the central galaxy (Rees & Ostriker 1977; Silk 1977; Binney 1977, White & Rees 1978). Gas that has never been shock heated close to virial temperature falls onto the galaxy from outside the virial radius along filamentary structures (e.g. Kereš et al. 2005). This latter mode is termed “cold mode” accretion, and is believed to be the dominant way of gas accretion for galaxies in low mass dark matter halos (Kereš et al. 2005, Dekel & Birnboim et al. 2006). Numerical studies characterise the filaments of cold mode accretion as cool and clumpy clouds surrounded by ionised gas (Kereš & Hernquist 2009).

There have been many observational attempts to trace the cold mode accreting gas around galaxies. Most of the evidence comes from observing ionised gas at intermediate to high redshift. QSO absorption lines in Mg II with an inflowing velocity feature have been found to be prevalent at a distance of tens of kpc around star forming galaxies (e.g. Giavalisco 2011, Kacprzak et al. 2012). At least one of them is observed to have a filamentary structure (Rauch et al. 2011). Furthermore, metal-poor Lyman limit systems are observed to have characteristics expected for cold accretion (Lehner et al. 2013).

Tracing the cold-mode accreting gas in the neutral phase in galaxies at low redshift has been difficult. HI clouds that form a filamentary structure have been found around some nearby galaxies (e.g., Shostak & Skillman 1989; Oosterloo et al. 2007; de Blok et al. 2014, for a review see Sancisi et al. 2008) and in the Milky Way (HVCs, Putman et al. 2002) but are more likely to trace interaction with companions and star formation feedback. None of them has been confidently demonstrated to be tracing cold-mode gas accretion. Although cold-mode accretion is believed to produce the highly clumpy galactic disks observed at high redshift (Agertz et al. 2009), we do not find an especially clumpy morphology for the HI-rich galaxies when compared to control galaxies at low redshift (J. Wang et al. 2013, 2014). This may be because at low redshift the accreting gas gets slowed down and blends better with the hot halo gas around the galaxies (Putman et al. 2012). Hence, it may be better to search for the cold-mode accreting neutral gas well outside the galactic disks, by searching for signal from a large volume around the central galaxies. Here we attempt to perform exactly this search by analysing the data taken as part of the Bluedisk project (J. Wang et al. 2012) in a special way.

Previous analysis of the same Bluedisk dataset already shows that the gas richness of a galaxy is linked to the gas richness of its environment. In particular, the satellites of abnormally HI-rich spirals are themselves abnormally HI rich (E. Wang et al. 2015). This result may be seen as a new manifestation of the “conformity phenomenon”, whereby the colours of satellites correlate with the colour of central galaxies (Weinmann et al. 2006, Kauffmann et al. 2010, W. Wang et al. 2012). The work of E. Wang et al. (2015) was based on individual HI detections in the Bluedisk data cubes and, therefore, is limited to galaxies with $M_{\text{HI}} > 10^8 M_{\odot}$. As previously pointed out by Kauffmann et al. (2010), because the galactic conformity usually extends to scales far beyond dark matter halos, it implies that the satellite galaxies are probably tracing the underlying smooth gas reservoir that

is available for fuelling the central galaxies. If this hypothesis is true, the conformity behaviour should still hold when it is examined at low luminosity levels (i.e. by tracing the less bright satellites or clouds in the general environment that are potentially far more numerous than the brighter satellites).

Motivated by these results we perform a new analysis of the Bluedisk data. Our aim is to trace the faint gas distribution that may surround galaxies below the detection limit of the HI data. Our method consists of adding up the flux of (both positive and negative) noise peaks in the HI data cubes out to a radius of 16 arc min (typically 500 kpc), trying to detect a statistical HI signal (i.e. an excess of positive detections) and studying whether its properties correlate with the HI content of the central galaxy.

The paper is organised as follows. In section 2, we describe the Bluedisk data used in this analysis. In section 3, we introduce our new method to measure a total HI mass in faint systems around primary galaxies through examining the noise peaks. In section 4, we discuss the origin of the HI mass measured from an analysis of the noise peaks. We find that the excess HI mass fraction in the primary galaxies is correlated with an excess HI mass in the surrounding environment. In section 5, we discuss the implication of our results for cold mode gas accretion in galaxies. A Λ CDM cosmology with $\Omega_m = 0.3$, $\Omega_{\lambda} = 0.7$ and $h = 0.7$ is assumed throughout the paper.

2 THE SAMPLE

2.1 The Bluedisk dataset

The Bluedisk project aims at searching for clues about gas accretion and galactic disk formation in the local universe. Details about the sample, data processing and analysis can be found in Paper I and II, and here we only review the most relevant information.

The sample consists of 50 massive galaxies ($M_{\star} > 10^{10} M_{\odot}$) with a redshift between 0.018-0.03 (corresponding to a luminosity distance of 70-130 Mpc). From the atlas in Paper I, most of them are blue spiral galaxies. The target fields are covered by the Sloan Digital Sky Survey (SDSS, Abazajian et al. 2009), the Galaxy Evolution Explorer (GALEX) imaging survey (Martin et al. 2005), and the Wide-Field Infrared Survey Explorer (WISE, Wright et al. 2010), allowing a multi-wavelength analysis. Radio 21 cm synthesis data were obtained with the Westerbork Synthesis Radio Telescope (WSRT), with the main goal of observing the HI emission line. In this paper, we make use of the HI data cubes optimised for high sensitivity at lower resolution, which are produced with Robust 0 weighting and 30" tapering. The data cubes have a typical rms of 0.37 mJy beam⁻¹, a typical beam size of 38" × 36" and a velocity resolution of 12.3 km/s (after Hanning smoothing), which provides sufficient sensitivity to detect point sources down to an HI mass of a few $10^8 M_{\odot}$. The primary beam has a FWHM (full-width-at-half-maximum) of $\sim 0.5^{\circ}$, corresponding to a ~ 1 Mpc sky region around the target galaxies, hence the data is very suitable for studying the relatively large-scale HI environment around the central sources. The details of the primary beam correction are discussed in E.Wang et al.(2015).

Following Paper I, we use the 42 isolated target galaxies for this study. Hence, the local environment is different from groups or clusters, where the dominant process is gas stripping rather than accretion. We further exclude two galaxies (galaxy 14 and 27) with the lowest redshift, so that we have a narrow redshift range of 0.023–0.03 (a luminosity distance of 100–130 Mpc). We call these 40 target galaxies “primary galaxies”.

These galaxies have a broad distribution in HI mass fraction $f_{\text{HI}} = \log M_{\text{HI}}/M_*$, ranging from lower than -2 to higher than 1 (Figure 1). Compared to other samples featuring HI-rich galaxies (like the samples from Lemonias et al. 2014 and the HIghMass project, High HI Mass, Huang et al. 2014), the Bluedisk sample has the advantage of being able to compare the most HI rich galaxies with those of normal HI content. As we will show later in Section 4.2, this is crucial for producing our main results.

As mentioned before, the aim of the paper is to investigate the connection between the HI in the (central) primary galaxies and the HI in the environment. In addition to f_{HI} , we also use a few other parameters to quantify the HI richness of primary galaxies. Using the GALEX Arecibo SDSS Survey (GASS, Catinella et al. 2010), Catinella et al. (2013, **C13 for short hereafter**) calibrated a photometric estimator of f_{HI} in galaxies with $\text{NUV}-r < 4.5$ (which is also the colour range of the Bluedisk sample). The estimator is a combination of the $\text{NUV}-r$ colour and the mass surface density, reflecting the connection between star formation rate and cold gas content. The difference between the observed and the estimated f_{HI} , which we denote as $\Delta_{\text{C13}f_{\text{HI}}}$, measures the excess gas, and can be used to indicate HI richness. Xiao et al. (in prep) further add the optical concentration parameter and stellar mass to the estimator, giving more control on the internal structure of galaxies. We also use the difference from this 4-parameter (4p) estimator ($\Delta_{4p}f_{\text{HI}}$) as a measure of HI richness.

3 METHOD

As discussed in the introduction section, the conformity behaviour of central and bright satellite galaxies can be interpreted in terms of an underlying extended reservoir of cold gas. If this hypothesis is correct, we expect to detect conformity also at lower HI mass levels than probed by E. Wang et al. (2015), in a regime dominated by very faint satellite galaxies and/or gas clouds in the inter-galactic medium. In this section we introduce our technique to detect this faint HI gas, in the environment of the Bluedisk galaxies.

The method entails an analysis of the noise peaks (both positive and negative) in **the cleaned data cubes** in order to obtain a statistical detection. Because the noise is distributed symmetrically around 0 (both the median and mean background of a cube are typically within $\pm 10^{-5}$ mJy beam $^{-1}$, while the rms of a cube is ~ 0.4 mJy beam $^{-1}$), a positive noise peak will statistically be cancelled out by a negative noise peak of the same level. If in addition to noise there is a collection of very faint HI objects, then these will add a slight positive signal to the noise, that will elevate the positive noise peaks or diminish negative noise peaks. This bias is detectable by a careful analysis of the distribution of the noise values throughout the cube. We do this by

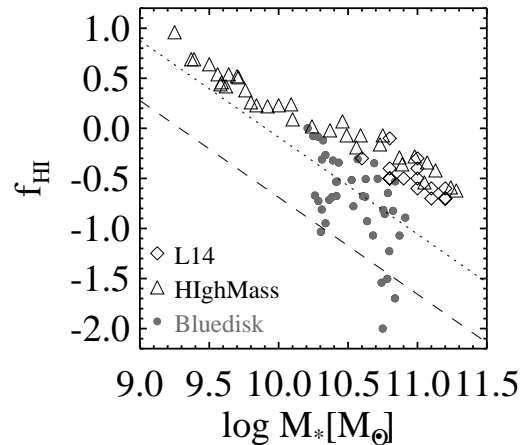


Figure 1. HI mass fraction of the Bluedisk sample (dark grey dots), the HIghMass sample (triangles), and the sample from Lemonias et al. (2014) (L14, diamonds). The dashed line shows the median relation between f_{HI} and stellar mass for general galaxies, taken from Catinella et al. (2010). The dotted line is the dashed line 0.6 dex upward, showing the original division between the Bluedisk high f_{HI} and control galaxies.

selecting all (positive and negative) noise peaks above 4σ in the area of interest, after removing the signal that has been reliably detected in the source finding procedure (see section 3.2).

Selecting noise peaks above a certain threshold has an important advantage compared to integrating over all voxels within a large area. Bright HI emission as well as diffuse faint HI emission in the data cubes is cleaned by means of clean masks (Paper I). The clean masks do not include the faint noise peaks used for our statistical analysis here, and these are therefore not cleaned. Because the integral over the **dirty beam** over a large area goes to zero it becomes very difficult to determine fluxes over extended areas without proper deconvolution. This is inherent to the sidelobe structure of the PSF. Any blind measurement of the total flux over a large area is therefore fraught with problems. However, by pre-selecting noise peaks, we analyse only the central part of the PSF and exclude any sidelobes. We are therefore unable to detect the HI mass of a very extended, smoothly distributed medium, (this is a consequence of using an interferometer with limited short baselines), but we are able to detect small scale faint emission using the method outlined here.

In the following sections, we describe our procedure in details. We improve the data quality by flattening the spectral baselines (section 3.1). We use the source-finding application SoFiA (Serra et al. 2015) to extract all signal exceeding 4σ . After removing all bright, reliable detections (section 3.2), we are left with “noise” peaks which we analyse in order to detect a statistical signal. We perform a series of careful tests to examine the robustness of the accumulative signal against various data reduction artefacts (section 3.3).

3.1 Flattening the spectral baselines

In order to improve the quality of the HI data cubes we fit second-order polynomial functions in moving windows along each line of sight. This allows us to obtain global functions describing the shape of the spectral baselines without specifying their functional form. In practice, we convolve each spectrum with the Savitzky-Golay filter (S-G, Savitzky & Golay 1964), an analytical solution for the local fitting process. We adopt a S-G filter with a half width of 70 channels (840 km/s), wider than the velocity width of all the galaxies in our data cubes. This ensures that the smoothed spectrum describes the large-scale shape of the baseline only. In Figure 2 we show the shape of the filter and demonstrate the convolution effect on simple functions, including the presence of edge effects. Within our analysis range of ± 500 km/s around the spectrum centre (channels 34 to 114), the S-G filter conserves the shape of the functions with a maximum deviation of less than 15%.

Before convolving the HI spectra with the S-G filter we mask channels that belong to one of the HI detections presented in Paper I (see also Sec. 3.2 below). We refer to these channels as the initial flagging set, and replace them with values interpolated from a first order polynomial fitting to the un-flagged part of spectrum. We calculate σ_m , the median absolute deviation of the original spectrum from the convolved spectrum, and update the mask by including all channels that deviate by more than $\pm 3 \sigma_m$ from the convolved spectrum. A flagged channel is replaced by the value interpolated from a first order polynomial fit to the un-flagged part of the whole spectrum, if it is in the initial flagging set, or in a flagged region that is wider than 10 channels and less than 40 channels from one end of the spectrum (potential bright sources that lie near the edge of the spectrum and cause incorrect continuum over-subtraction during the former data reduction). Otherwise the flagged channel (which is not likely to belong to a bright source) gets replaced by a first order polynomial interpolation from nearby channels. We repeat the above steps of flagging and convolution until σ_m (with typical value of a few times $0.1 \text{ mJy beam}^{-1}$) varies by less than $10^{-5} \text{ mJy beam}^{-1}$, or after 10 iterations. Figure 3 shows that this procedure models a variety of spectral baseline shapes successfully.

The final step of this procedure consists of combining all spectral baseline models into individual cubes. We smooth these cubes with a gaussian kernel with a FWHM of 2 pixels in the Ra-Dec direction in order to reduce the fluctuation between adjacent pixels (this does not significantly modify the PSF (which has a typical FWHM of 3.7 pixels)). Finally, we subtract the resulting spectral baseline model cube from the original cube. After this subtraction, the median rms of each data cube drops very slightly from 0.367 to $0.363 \text{ mJy beam}^{-1}$ (and from 0.372 to $0.362 \text{ mJy beam}^{-1}$ for the inner channel range 34 to 114). Hence while flattening the baselines, the method does not significantly change the global noise properties of the cube. In Figure 4, we compare two data cubes, using the same position-velocity cut, one as obtained before the additional continuum subtraction, and one as obtained after the additional continuum subtraction. While the noise features look similar, the continuum subtraction is obviously improved.

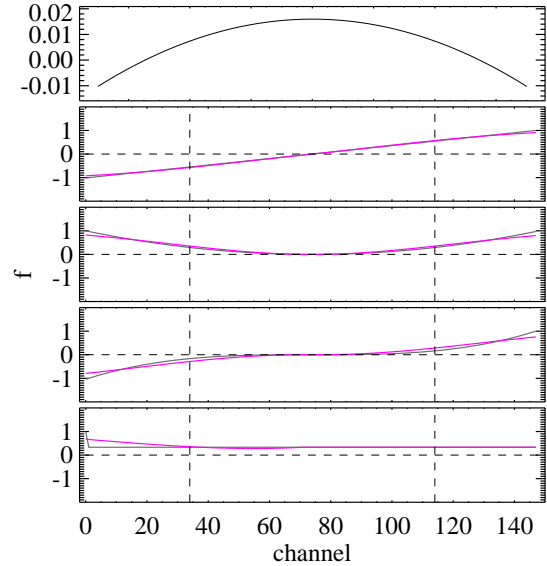


Figure 2. The S-G filter (top row) and examples of the convolution effect on simple functions. The area under the S-G filter in the top row is normalised. From the second to the bottom row, the dark grey curves are linear, second order polynomial and third order polynomial functions and a flat line with a spike on one side. The magenta curves are the result of the grey curves convolved with the S-G filter. The horizontal dashed lines mark the y axis position of 0, and the vertical lines mark the channels 34 and 114.

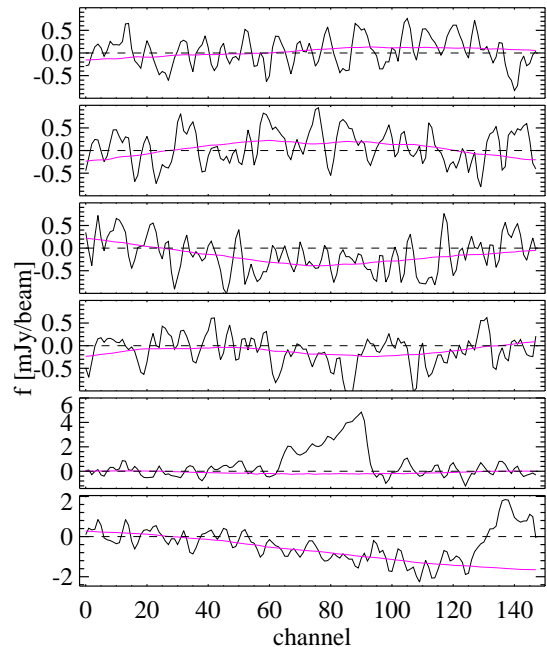


Figure 3. Examples of spectra before (black lines) and after applying the S-G filter (magenta lines). The dashed lines mark the zero level.

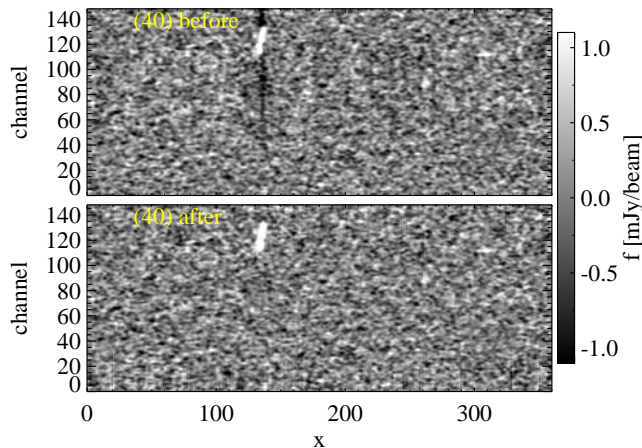


Figure 4. An example of an x - z projection from an original HI cube (top) and that after applying the improved continuum subtraction discussed in section 3.1 (bottom). The displayed grey scale ranges from -3 to 3σ around the mean of the cube.

3.2 Source finding and statistical detection of HI in the environment

We extract sources (both real detections as well as noise peaks to be used for our statistical analysis) from the improved HI data cubes¹ using the source detection software SoFiA². We refer to Serra et al. (2015) for a detailed description of the software. Here, we only outline the most relevant steps and describe the key parameter choices.

SoFiA first convolves the data with various smoothing kernels and selects voxels with absolute values above a certain threshold. We use smoothing kernels with a width of 0 and 3 pixels in the projected sky direction (roughly the size of the synthesised beam), and a width of 0, 3 and 5 pixels (corresponding to 0, 36 and 60 km/s) in the velocity direction (smoothing with a kernel with width of 0 is equivalent to no smoothing). Each channel of the cube is weighted according to the noise, so that noise variations along the velocity axis are removed. This step is very useful to suppress the detection of weak RFI (radio frequency interference) residuals. We adopt a detection threshold equal to 4σ . We note that the clipping is performed on the absolute values of the voxels in the filtered data cubes, meaning that our initial source list contains sources with negative total flux. These parameter settings for SoFiA are chosen after several tests and provide a good balance between suppressing the noise and gathering sufficient statistics for the following analysis..

SoFiA calculates a reliability index R for each source with positive total flux (Serra et al. 2012, 2015). We chose $0.01 \text{ Jy beam}^{-1}$ as a minimum total flux and $R > 0.99$ to classify a positive detection as a reliable source. We will refer to the remaining positive and negative detections (the noise peaks) as the “candidates” hereafter. While the division between reliable sources and candidates is not strict, we will see in section 4.1 that the candidates close to the thresh-

old of reliable sources do not dominate the total signal in candidates.

Using these selection criteria, besides the 40 primary galaxies, SoFiA detects in total 59,757 sources from the 40 cubes, of which, using the scheme as described, 137 are classified as reliable. 42 of the reliable sources lie within a projected distance (D_{proj}) of 500 kpc and a systematic velocity difference (ΔV_{sys}) of 500 km/s around the primary galaxies. 95% of them have $M_{HI} > 1.62 \times 10^8 M_{\odot}$. All of them can be associated with an optical galaxy down to a r band magnitude of 22 by requiring the centre to be offset by less than the size of the HI beam. The connection between primary galaxies and these reliable sources (satellite galaxies) is studied in detail in E. Wang et al. (2015). One of the key findings is that the satellites of HI-excess galaxies ($\Delta_{C13} f_{HI} > 0$; see Sec. 2) have higher HI excess than the satellites of HI-normal galaxies ($\Delta_{C13} f_{HI} < 0$). Here we aim to test whether such a connection between the HI content of galaxies and that of their environment holds also when studying the fainter, candidate HI sources.

We find 6,369 candidates that lie within a D_{proj} of 100 to 500 kpc and V_{sys} distance of 500 km/s from the primary galaxies, and these will serve as the main sample for analysis in what follows. We exclude the inner 100 kpc region because some of our HI rich galaxies have large HI disks extending to ~ 100 kpc. The radial range is always confined within the full-width-half-power of the primary beam. Most of the candidates have HI masses (absolute values for the negative candidates) within the range of $4.0 \times 10^6 M_{\odot}$ and $1.4 \times 10^8 M_{\odot}$ (5 and 95 percentiles of the distribution).

The ensemble of all positive and negative candidate detections results in a net positive HI signal in the environment around Bluedisk galaxies. We show this by calculating for each cube the accumulative HI mass ($M_{HI,cand}$) by summing up all negative and positive candidates in the volume defined above. To further improve the signal-to-noise ratio, we calculate the average $M_{HI,cand}$ of the 40 cubes. We calculate the error bars as a combination of the variation over the data cubes (var1) and the mean variation within a data cube (var2). The variation over the data cubes (var1) is calculated through a standard bootstrapping procedure. Taking the whole sample of 40 cubes for example, we randomly select 40 cubes from the sample (repetition allowed) and calculate the average $M_{HI,cand}$. We repeat this step for 1000 times and obtain a distribution consisting of 1000 values of average $M_{HI,cand}$. var1 is calculated as the variation of this distribution. The final error is calculated as $\sqrt{var1 + var2}$. We derive an average $M_{HI,cand}$ of $\sim 1.1 \times 10^8 M_{\odot}$ for the 40 cubes within the whole analysis volume.

The question is, however, whether and how significantly $M_{HI,cand}$ is affected by remaining artefacts in the data. Asymmetrically distributed noise can come from weak RFI residuals that are not completely removed during data reduction, and can also be produced in the continuum subtraction and cleaning processes. Hence in the following subsections we undertake a series of tests to identify and quantify these effects, before moving on to the scientific interpretation in section 4.

¹ The data cubes are not corrected for primary beam attenuation. The HI mass of sources are corrected for the primary beam attenuation after they are extracted.

² <https://github.com/SoFiA-Admin/SoFiA>

3.3 Influence of synthesis data reduction on the mass in candidates

We begin this series of tests by verifying that the white noise in the data does not accumulate to a significant net signal. We test this by applying the same source finding and $M_{\text{HI,cand}}$ measurements presented in section 3.2 to the Stokes Q cubes. Since no polarised signal in the line data is expected, the result is expected to be 0 unless indeed a positive accumulative noise signal is present. Figure 5 confirms that $M_{\text{HI,cand}}$ of the Stokes Q cubes is indeed close to 0.

In addition, we visually inspect the data cubes carefully in various projections. The well trained eye is able to spot and identify systematics in the data. Because the WSRT is a linear E-W array, bright RFI residuals show patterns of parallel stripes and bright cleaning residuals show patterns of elliptical rings around bright sources on the Ra-Dec projections. Improper continuum subtraction results in negative regions on the Ra-velocity or Dec-velocity projections (see Figure 4). We find no obvious cleaning or continuum subtraction residuals. We find some very weak underlying RFI patterns in a few channels, but none of our HI candidates are associated with any of those. This is partly because the source finder takes into account noise variations within cubes (including those caused by residual RFI; section 3.2)

We continue our search for possible sources of systematic error in our measurement of $M_{\text{HI,cand}}$ by investigating the effect of incorrect cleaning and continuum subtraction. Any systematics related to clean residuals (**i.e. the presence of residual side lobe flux in the HI cubes**) should correlate with a higher cleaned flux or a larger cleaned region. This opens the possibility for the following tests.

We calculate the sum of all positive voxels belonging to candidates and the absolute sum of all the negative voxels belonging to candidates, and we refer to them as f_{+cand} and f_{-cand} . We calculate the total flux in the reliable sources and the total flux in the candidates, and refer to these as f_{rel} and f_{cand} respectively. We calculate f_{+cand} , f_{-cand} , f_{cand} and f_{rel} for each channel map within 500 km/s from the systemic velocity and 500 kpc from the position of the primary galaxy. These are the velocity range and sky region within which we perform our analysis. The top row of Figure 6 shows that there is no correlation between f_{-cand} and f_{rel} , suggesting that clean residuals do not significantly affect the noise (negative voxels) of the data cube. There is a very weak relation between f_{+cand} and f_{rel} , resulting in a systematic linear relation of f_{cand} increasing slightly as a function of f_{rel} . We argue that part of the relation reflects galaxy-environment connections rather than artefacts, as we will show later. If we attribute the relation fully to clean artefacts around reliable sources, on average an HI mass of $0.11 \times 10^8 M_{\odot}$ related to clean artefacts is present in each data cube, which is an order of magnitude lower than the average HI mass contained in the candidates ($M_{\text{HI,cand}} \sim 1.1 \times 10^8 M_{\odot}$, section 3.2). In the bottom row of Figure 6, we perform a similar analysis as in the top row but replace f_{rel} with N_{rel} , the number of voxels in the reliable sources. We get similar trends, and the linear relation between f_{cand} and N_{rel} suggests that on average a maximum positive bias in HI mass of $0.07 \times 10^8 M_{\odot}$ is associated with the cleaning of reliable sources in a data cube. These tests demonstrate that the cleaning process may indeed leave a

small amount of positive residual flux, but it does not significantly affect $M_{\text{HI,cand}}$ of the candidates.

Are there faint systematic residuals from continuum subtraction that can not be directly caught by eye? We extract continuum sources from the continuum maps, with a 3σ detection threshold. These sources have a 5 percentile of 0.94 mJy in the flux distribution. We find that 99% of the flux in candidates comes from sight lines without detectable continuum sources. The fraction is higher than 95% for both positive and negative candidates, if we count them separately. Hence continuum subtraction residuals are not likely to significantly affect $M_{\text{HI,cand}}$.

We also find that the flux in candidates is not correlated with radio flux in continuum sources (with a Pearson correlation coefficient of 0.06) or the number of continuum sources (with a Pearson correlation coefficient of -0.27). We divide the galaxy sample equally into two subsets by the total flux in continuum sources, maximum flux in continuum sources and number of continuum sources, and compare their $M_{\text{HI,cand}}$ (see Figure 7). We find no differences for data cubes having different values for the total or maximum radio flux present in the form of continuum sources. There is a trend that data cubes with fewer radio continuum sources have higher $M_{\text{HI,cand}}$. However, the number of background continuum sources does not correlate with any of the galaxy properties discussed in section 4.2, and we conclude that this correlation does not affect our main results.

Finally, we note that cumulatively there is a weak gradient of $M_{\text{HI,cand}}$ on the low and high V_{sys} sides of the primary galaxies, which is unlikely to be physical but does not significantly affect the main result of this paper. We refer the readers to Appendix A for a detailed investigation of this issue.

3.4 A summary of the method

To summarise, we used SoFiA to extract candidates with typical mass of $10^7 M_{\odot}$, which is lower than that of reliably detected sources but higher than most of the data reduction artefacts. We have shown that the total HI mass in candidates, $M_{\text{HI,cand}}$, is not sensitive to artefacts produced in the continuum subtraction and cleaning processes of our data reduction, and potentially traces a reservoir of low surface density HI gas in data cubes. In the following section we study the nature of these candidates and investigate whether $M_{\text{HI,cand}}$, i.e., the gas mass contained in the environment of Bluedisk galaxies, correlates with properties of the primary galaxies.

4 RESULTS

4.1 The nature of the HI mass in candidates

In this section, we attempt to understand better the nature of the signal in the cumulative $M_{\text{HI,cand}}$ around the Bluedisk primary galaxies. From the top row of Figure 8, we can see that the average profile of $M_{\text{HI,cand}}$ around the 40 primary galaxies rises steadily to $\sim 1.1 \times 10^8 M_{\odot}$ from a projected distance of 100 kpc out to 500 kpc, and from a systematic velocity distance of 0 out to $\sim \pm 300$ km/s. In the bottom-left panel, the accumulative $M_{\text{HI,cand}}$ is plotted as a func-

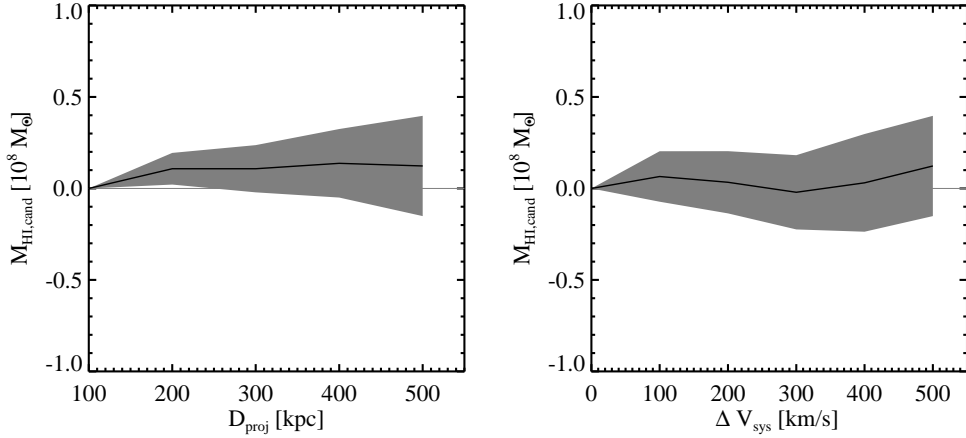


Figure 5. The average accumulative $M_{\text{HI,cand}}$ from Stokes Q cubes as a function of projected distance (left) and systematic velocity distance (right) to the primary galaxies. The solid black lines show the average profiles around each primary galaxy, and the grey shades show the errors.

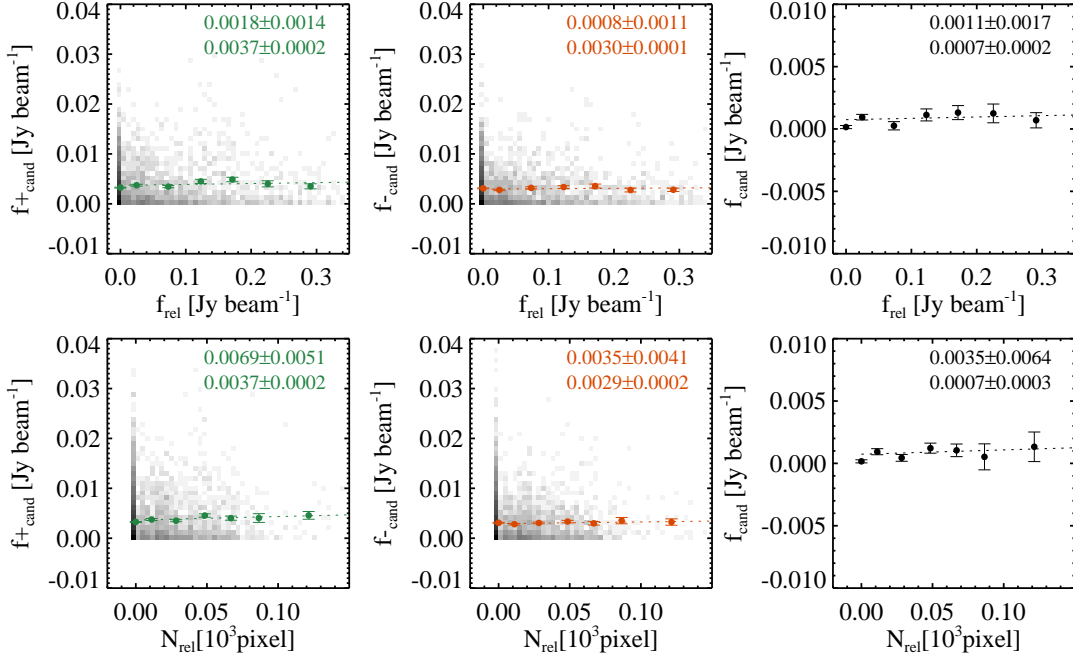


Figure 6. Relations of fluxes in candidates and the reliable sources in channels. f_{+cand} is the total flux of positive voxels in candidates, and f_{-cand} is the absolute total flux of negative voxels in candidates. f_{rel} and N_{rel} are the total flux and voxel number in reliable sources. In each panel, the grey scale map shows the number density of data points, the dots with error bars represent the mean values in each x-axis bin, and the dotted line shows a linear fit to the dots, with slope and intercept of the fit denoted (in the first and second row, respectively) on top of the panel.

tion of absolute HI mass of individual candidates, and we can see that $M_{\text{HI,cand}}$ is not dominated by the most massive candidates. The candidates with $M_{\text{HI}} > 10^8 M_{\odot}$ contributes only $\sim 1/3$ of the net signal. We extract the spectra for all the candidates, shift them to have the same central systematic velocity of 7700 km/s, and stack them. The stacked spectrum, as displayed in the bottom-right panel of Figure 8, is a narrow emission line with a gaussian fit σ of 18.9 ± 5.7 km/s. Removing the resolution effect, the line has a width of $\sigma \sim 14.3$ km/s. If we assume rotational systems and apply this velocity width to the baryonic Tully-Fisher relation (McGaugh et al. 2000), it corresponds to a baryonic

mass of $4.4 \pm 2.5 \times 10^7 M_{\odot}$, similar to the typical M_{HI} of a positive candidate. The candidates could be low mass satellite galaxies, HI clouds, or HI clumps in low surface density HI disks.

If part of $M_{\text{HI,cand}}$ probes HI in galaxies, we expect the positive candidates to trace galaxies more closely than the negative candidates. As a test, we select galaxies with r band flux brighter than 20 mag from the SDSS DR7 photometric catalog. For each candidate we search for the optical galaxy with the smallest projected distance. We compare the distribution of matching distances for the positive candidates, the negative candidates and simulated random positions. In the

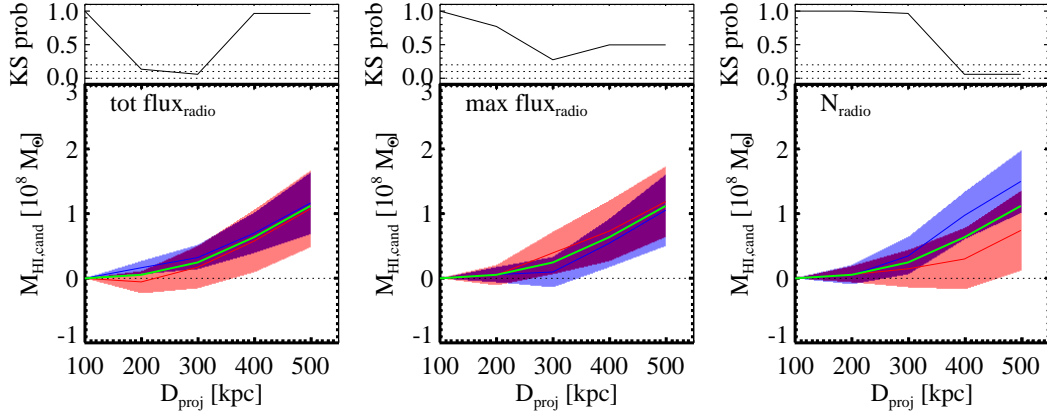


Figure 7. Averaged accumulative $M_{\text{HI,cand}}$ as a function of distance between 100 and 500 kpc from the primary galaxies. In each panel, the primary galaxies are evenly divided into two sub-samples by the median value of the parameter denoted in the left-top corner. The red colour is for the sub-sample with higher values of the dividing parameter, and the blue colour is for the comparison sub-sample with lower values. The solid lines running through coloured shades show the mean $M_{\text{HI,cand}}$ with error bars. The green line shows the averaged $M_{\text{HI,cand}}$ for the whole sample of 40 cubes, to guide the eyes. The black dotted lines show the position of zero HI mass. The top of each panel shows the KS-test probabilities as a function of radius comparing the distribution of surrounding HI mass in the two sub-samples. A KS-test probability of 0.1 means that there is 90% significance that the two distributions are different.

left panel of Figure 9, the negative candidates closely follow the curve for random positions (with a K-S test probability of 0.95, meaning that at a 5% significance the null hypothesis of the two distributions being drawn from the same parent distribution can be rejected). We find that a slightly higher fraction of positive candidates can be matched to optical galaxies than the negative candidates at small matching distance (< 50 arcsec, ~ 1.5 times the FWHM of the HI PSF), although a K-S test probability of 0.28 suggests the difference is not strong. If we further take only the positive candidates with $M_{\text{HI}} > 1.25 \times 10^7 M_{\odot}$ (70 percentile in the mass distribution of positive candidates; based on the bottom-left panel of Figure 8, these are the candidates that contribute nearly all the net $M_{\text{HI,cand}}$ signal) into account, we find a significant difference in the distribution of matching distances from the negative candidates (K-S test probability ~ 0.04) and from the simulated random positions (K-S test probability ~ 0.01). We further check if this small excess of optical matches for the bright positive candidates might be due to residual from the continuum subtraction around continuum sources associated with the optical sources. In the middle panel of Figure 9, we match the projected position of negative, positive and bright positive candidates to continuum sources. We find the three types of candidates to be indistinguishable in the distribution of matching distances when the distance is smaller than 50 arcsec. The K-S test probability is 0.98 for the comparison between negative and positive candidates. The K-S test probability is 0.14 for the comparison between negative and bright positive candidates, suggesting a weak difference, but the curve shows that the bright positive candidates are less likely to be found along sight lines of continuum sources than the negative candidates. Hence we can conclude that at least the brightest $\sim 1/3$ of the positive candidate sample appears to be connected to galaxies, but not necessarily radio bright galaxies.

We also expect the positive candidates to have a broader line width than the negative candidates if they are more likely to be associated with galaxies. This expectation is confirmed in the right panel of Figure 9. The K-S test probabil-

ity is 7×10^{-6} for comparison between positive and negative candidates, and is 0.04 for comparison between the positive and negative candidates with absolute $M_{\text{HI}} > 1.25 \times 10^7 M_{\odot}$.

In summary, by measuring $M_{\text{HI,cand}}$, we add up the signal from unresolved, low HI mass objects distributed in a large volume (~ 500 kpc) around the primary galaxies and other reliably detected objects. It is very likely that at least a fraction of these candidates are small galaxies. The remainder might be galaxies too (e.g., objects below the 20 mag cut in r band used here), or small HI clouds in the circumgalactic medium.

4.2 The HI mass in candidates and the properties of primary galaxies

In this section, we compare $M_{\text{HI,cand}}$ between galaxies with different properties, especially between galaxies that are rich in HI and normal galaxies. We assume that the HI-rich (either with high f_{HI} or HI excess) galaxies have been accreting gas, and hope to find clues about gas accretion by studying $M_{\text{HI,cand}}$ around the galaxies.

In Figure 10, we divide the sample of primary galaxies evenly into two sub-samples, focusing on different properties, and investigate their difference in averaged accumulative $M_{\text{HI,cand}}$ as a function of D_{proj} between 100 and 500 kpc. The dividing galactic properties include the stellar mass (M_{\star}), the stellar mass surface density (μ_{\star}), optical concentration (r_{90}/r_{50}), NUV-r colour, the HI mass (M_{HI}), HI mass fraction (f_{HI}), and HI excess ($\Delta_{13}f_{\text{HI}}$ and $\Delta_{4p}f_{\text{HI}}$)¹.

The most prominent trend is the sub-sample with lower M_{\star} having higher $M_{\text{HI,cand}}$ than the comparison sub-sample, with a higher than 90% significance that the two distributions are different at a D_{proj} of 500 kpc. The sub-samples

¹ We point out the pairs of subsamples investigated here all have similar ranges of redshift (e.g. the difference in median luminosity distance is always less than 6%)

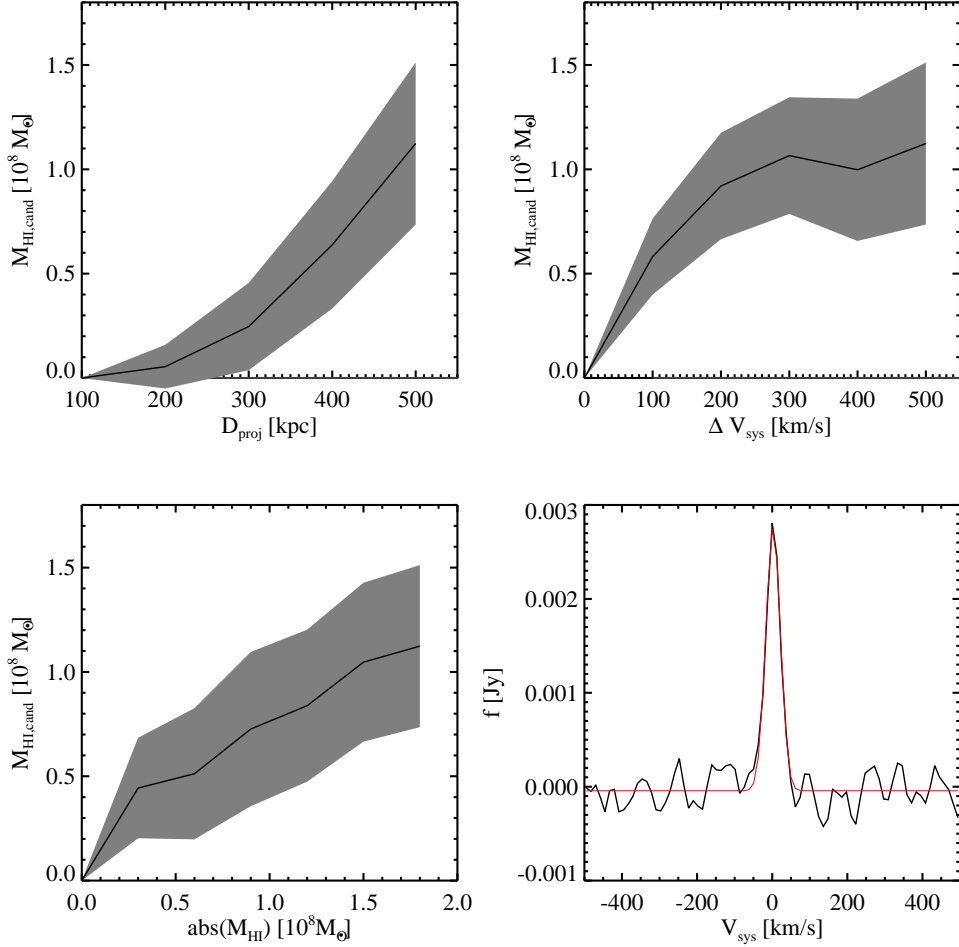


Figure 8. Top row and bottom-left panel: the average accumulative $M_{\text{HI,cand}}$ as a function of projected distance and systematic velocity distance to the primary galaxies, and as a function of the individual HI mass (absolute value) of candidates. The solid black lines show the average and the grey shades show the errors. Bottom-right panel: stacked spectrum of candidates (black line) and its gaussian fit (red line).

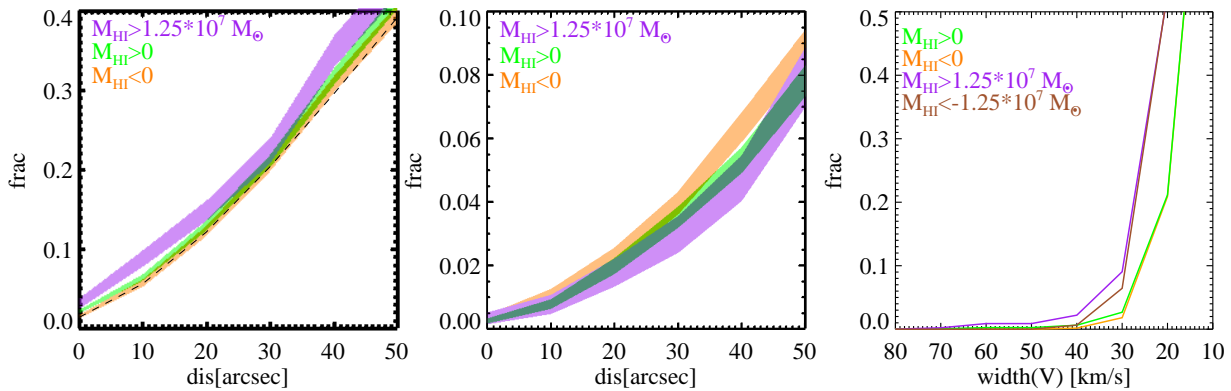


Figure 9. The onnection of negative (orange), positive (green) and bright positive (purple) candidates with optical and radio continuum sources. Left panel: accumulative fraction of projected distance between the candidates and their closest optical galaxies. The dashed line is built from matching simulated random positions with the optical galaxies. Middle panel: accumulative fraction of projected distance between the candidates and radio continuum sources. Right panel: accumulative fraction of velocity width (length of the detection mask in the velocity direction). The colours used for the different sub-samples are denoted in the left-top corner.

with higher f_{HI} and $\Delta_{4p}f_{\text{HI}}$ also have considerable higher $M_{\text{HI,cand}}$ than the comparison sub-samples; especially the latter has a close to 90% significance for the difference in distribution from the comparison sample. There are also weak trends that the sub-sample with lower μ_* and bluer NUV-r colour have higher $M_{\text{HI,cand}}$ (considering the difference in average values and the close-to 0.2 K-S test probabilities). There is no significant correlation between $M_{\text{HI,cand}}$ and the optical concentration, the HI mass or $\Delta_{C13}f_{\text{HI}}$ of primary galaxies.

We further control stellar mass to reveal a more intrinsic correlation between $M_{\text{HI,cand}}$ and HI richness of primary galaxies. For each of the sample dividing parameters, we derive the linear relation with stellar mass, and calculate vertical distance to the relation. We use this distance to divide the primary galaxies evenly into two samples, and study their difference in averaged accumulative $M_{\text{HI,cand}}$. In Figure 11, we only consider the dividing parameters which have already shown an indication for a correlation with $M_{\text{HI,cand}}$ in Figure 10. We can see the trend of galaxies with higher f_{HI} having on average higher $M_{\text{HI,cand}}$ becomes more prominent as suggested by the K-S test probabilities. The trend as a function of $\Delta_{4p}f_{\text{HI}}$ remains almost unchanged, suggesting the advantage of $\Delta_{4p}f_{\text{HI}}$ as an unbiased measure of HI richness. Bluer primary galaxies also have on average higher $M_{\text{HI,cand}}$. $M_{\text{HI,cand}}$ is no longer dependent on μ_* of primary galaxies. These trends are consistent with each other, for at the same stellar mass, HI-rich galaxies are also more star forming galaxies. Finally, we note that, when the sample is divided by f_{HI} , $\Delta_{4p}f_{\text{HI}}$ and NUV-r of the primary galaxies, the difference in the $M_{\text{HI,cand}}$ distribution of the sub-samples is tentative, with a K-S test probability of slightly above 0.1 at a D_{proj} of 300-500 kpc.

5 DISCUSSION: EVIDENCE OF GAS CONFORMITY

We have found evidence for the presence of an excess of faint gas clouds in a volume out to 500 kpc in projected distance and 500 km/s in velocity around HI excess galaxies, i.e., galaxies that have more HI mass than other galaxies with similar optical properties. A parallel study of individual satellite galaxies around the Bluedisk primary galaxies revealed that satellites around HI excess galaxies have higher HI excess than satellites around galaxies with normal HI contents (E. Wang et al. 2015). Although these two studies are based on different signal-to-noise levels of the HI data, reflecting different reservoirs of cold gas, they consistently tell the same story: the HI reservoir in the environment of (massive) galaxies appears to reflect the HI content of those galaxies. As discussed in K10, this environmental HI may trace the dense gas tunnelled into halos through filaments, the so-called ‘‘cold mode’’ accretion (Kereš et al. 2005).

Recent numerical studies have shown that cold mode accretion is not affected by galactic winds (Powell et al. 2011), hence it can easily leave its footprint on the low-mass satellite galaxies. Beside the gas locked into satellites, our HI candidates may also include the HI clouds that condense from the ionised cold mode gas (Kereš et al. 2009a, 2009b). It is interesting to note that the lower limit in the HI mass of candidates detected in our data ($\sim 10^6 M_{\odot}$, imposed by

our 4- σ detection threshold) is roughly the lower mass limit required by an HI cloud to survive in a hot gas halo around galaxies (Murray & Lin 2004). Due to the lack of baseline spacings short-ward of 36 m, we are unable to detect the very extended, smoothly distributed gas. However, the detected candidates that trace the peaks in the IGM or small companion galaxies, indicate that an underlying reservoir of gas from cold mode accretion might be present.

In the picture of cold mode accretion, the outer region of the galactic disks is the favoured location of the accretion taking place (as in the classical model of hot accretion) (Pichon et al. 2011). The accretion rate is bursty because the inflow filament is clumpy (Brooks et al. 2009). These two factors may produce the excess HI in HI-excess galaxies. The Bluedisk primary galaxies have stellar masses around that of the MW, for which around 50% of the gas accretion occurs in the cold mode (van de Voort & Schaye 2012). The most prominent trend found in this paper is that the primary galaxies with lower stellar masses have higher HI mass in candidates around them, which may suggest a transition between cold- and hot-mode accretion, as predicted by the simulations (Dekel & Birnboim et al. 2006). Recently Kauffmann (2015) found a tendency for the satellites to align along the major axis of late-type HI-rich central galaxies with $M_* < 10^{10.5} M_{\odot}$; they found no such phenomenon for more massive central galaxies. Their result also suggests such a transition. The median M_* of our primary galaxies ($10^{10.56} M_{\odot}$) is consistent with their suggested transition point.

An alternative picture is that the accumulative signal from HI candidates traces a rather smooth accretion of dark galaxies. Genel et al. (2010) studied the growth of dark matter halos and found that at least 40% of the baryons in the halos are accreted from very low mass halos, containing smooth cold $T \sim 10^4 \text{K}$ gas and no stars. Although no dark galaxies have been found so far from nearby surveys (Zwaan & Briggs 2000, Zwaan 2001, Koribalski et al. 2004, Haynes 2007), this can be explained if dark galaxies are preferentially found around gas accreting massive galaxies: galaxies with very high f_{HI} and as massive as the Bluedisk sample are rare in the nearby universe. This picture may still be consistent with the cold accretion scenario, since recent simulations show that halos in filaments may have more sub haloes than those in other environment (Guo et al. 2014).

To this date no gas accreting filaments or clouds have directly been observed to exist within a few tens of kpc around galaxies in the local universe, even when the observational depth reaches $10^{19} \text{ atom cm}^{-2}$, as in the case of the WSRT Hydrogen Accretion in LOcal GALaxies Survey (HALOGAS, Heald et al. 2011). However, numerical simulations demonstrate that the accreting gas may just get slowed down and ionised through interaction with the hot gas halo when it gets close to the galactic disks (Putman et al. 2012). In our study here, the candidates are beyond 100 kpc from the galactic centre, far above the disk-halo interface.

Finally, we address the question if the merging of satellites contributes significantly to the cold gas in primary galaxies. We select the 20 primary galaxies with higher than median f_{HI} , and only 8 of them have reliably detected satellites within a D_{proj} of 500 kpc and ΔV_{sys} of 500 km/s. We calculate the timescale for a pair of galaxies to merge follow-

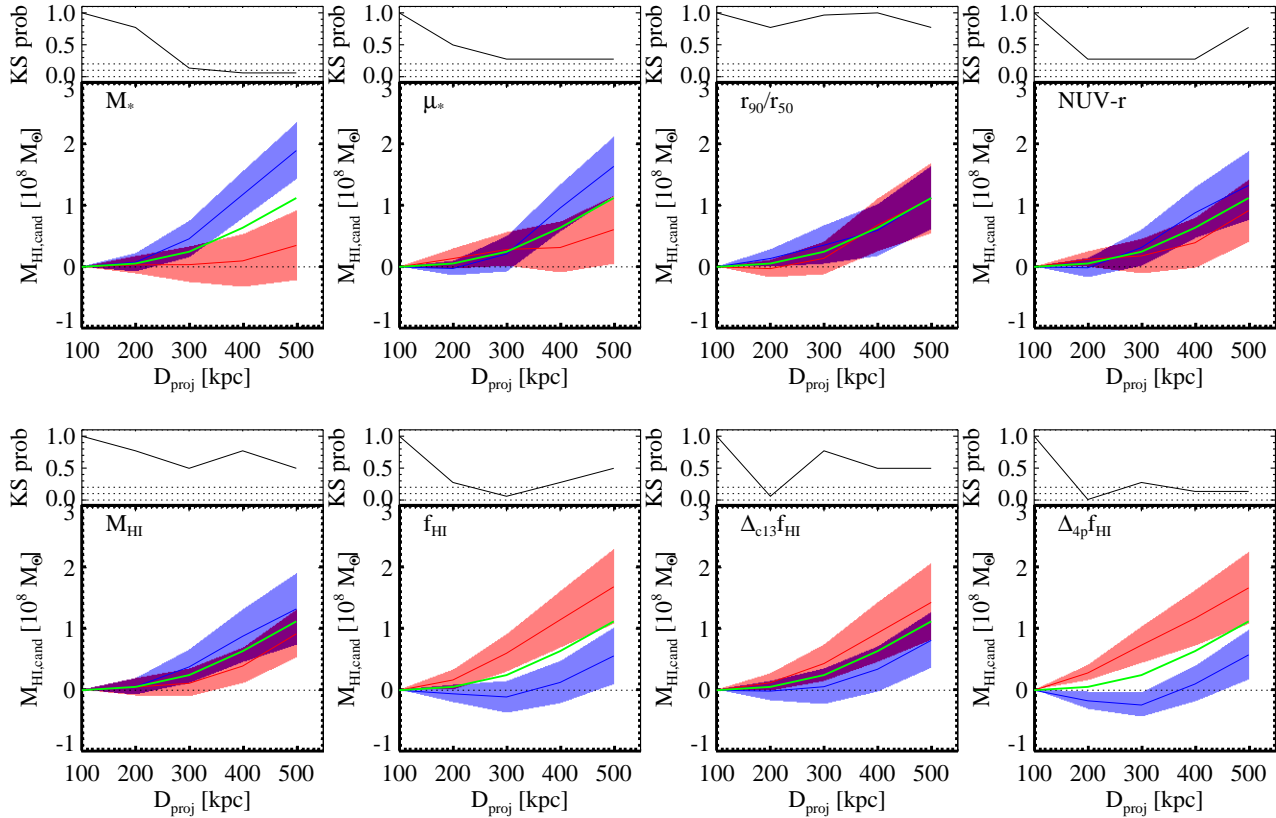


Figure 10. Averaged accumulative $M_{\text{HI,cand}}$ as a function of distance between 100 and 500 kpc from the primary galaxies. In each panel, the primary galaxies are evenly divided into two sub-samples by the median value of the parameter denoted in the left-top corner. The red colour is for the sub-sample with higher values of the dividing parameter, and the blue colour is for the comparison sub-sample with lower values. The solid lines running through coloured shades show the mean $M_{\text{HI,cand}}$ with error bars. The green solid lines show the averaged accumulative $M_{\text{HI,cand}}$ of the whole sample for guiding the eye. The black dotted lines show the position of zero HI mass. The top of each panel shows the KS-test probabilities as a function of radius comparing the distribution of surrounding HI mass in the two sub-samples. The dotted lines show the positions of 0, 0.1 and 0.2. A KS-test probability of 0.1 means that there is 90% significance that the two distributions are different.

ing the empirical formula from Kitzbichler & White (2008),

$$T = 1.6 \frac{r}{25h^{-1}\text{kpc}} \left(\frac{M_*}{3 \times 10^{10} h^{-1} M_\odot} \right)^{-0.3} \text{Gyr} \quad (1)$$

where M_* is the total stellar mass of the pair. We replace M_* in the formula with M_{HI} plus M_* to minimize the timescale. We calculate the gas merging rate, and compare it with the SFR for these 8 primary galaxies with satellites. The highest ratio is 0.12, hence the merging rate is too low to support the SFR, and can not be a major source for replenishing the gas storage in the Bluedisk HI-rich galaxies. It is consistent with the findings of many previous studies like K10 and Di Teodoro & Fraternali (2014).

The gas-rich satellites studied by K10 and E. Wang et al. (2015) might be the tip of the iceberg of the missing gas accretion. Here with the detection of an excess in the low-mass low-column density HI environment, we might have detected a substantial part of the iceberg below the sea-level.

6 SUMMARY AND FUTURE PROSPECTS

We have developed a new technique to extract information about the large-scale distribution of HI mass from 21 cm

synthesis data cubes through a technique similar to stacking, which works in an HI mass regime which is lower than achievable for reliable direct detections, but still high enough not to be dominated by data reduction artefacts.. We used our technique to investigate the mass contained in candidate HI sources, possibly associated with individual satellite galaxies, around the Bluedisk primary galaxies. We found a connection between HI excess ($\Delta_{4p}f_{\text{HI}}$, or high values of f_{HI} at a fixed stellar mass) in primary galaxies and excess of HI in low mass candidates in the surroundings. These HI masses may be the tip of the iceberg of an underlying extended reservoir of gas that fuels the primary galaxies. It is a direct detection of the galactic gas conformity phenomenon down to very low HI masses ($\sim 10^7 M_\odot$). The result is consistent with the cold mode accretion in cosmological simulations. In such a picture, primary galaxies and satellites are both fuelled by the cosmic web and exhibit the conformity phenomenon of gas richness. The unusually blue outer discs in Bluedisk galaxies with high HI mass fractions, indicating inside-out formation, can also be explained with such cosmological gas accretion (Kauffmann 1996).

At this moment, we are unable to establish general relations between the mass, structure and morphology of the stellar disks and the surrounding HI masses because we

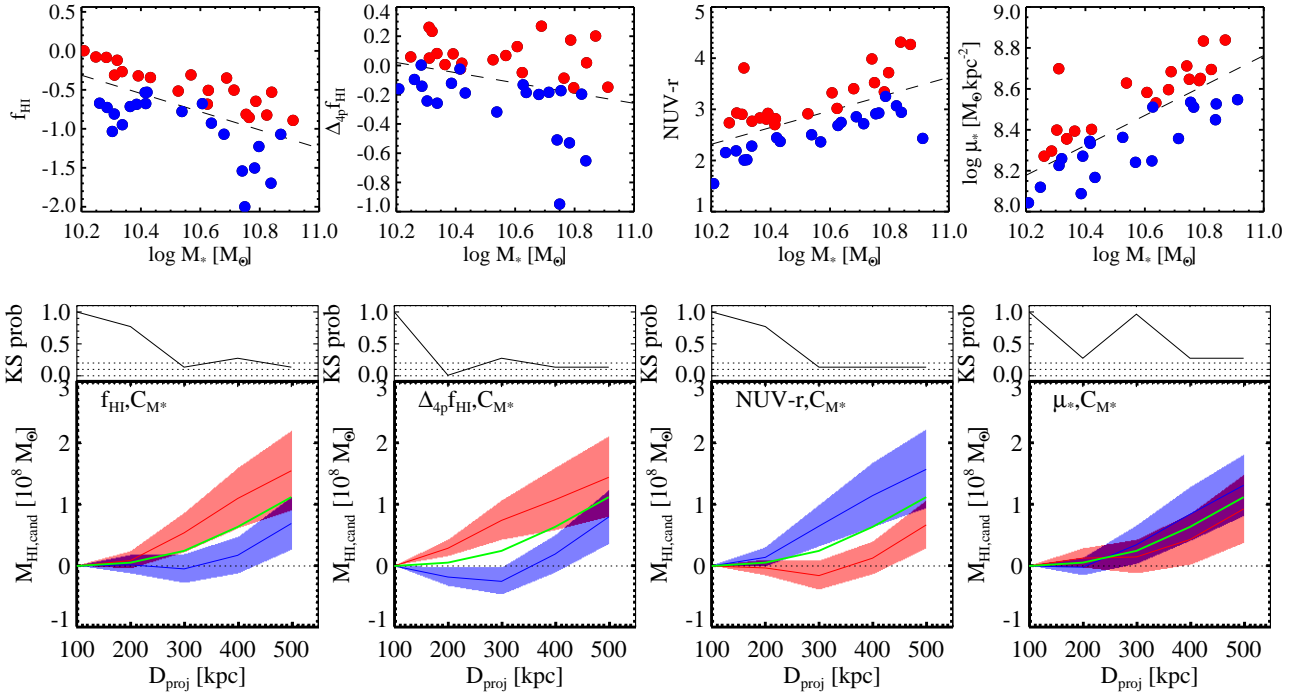


Figure 11. The top row demonstrate how the sample is divided with stellar mass controlled (see text). In each panel, the dashed line is the linear fit to the whole sample, and the red and blue dots are with vertical distance above and below the median to the dashed line. The bottom row is similar as Figure 10, but the sub-samples are divided with stellar mass controlled as shown in the panel on top.

are limited by selection effects in our sample of primary galaxies. Our sample misses the most massive galaxies (with $M_* > 10^{11} M_\odot$) in the universe. In more massive halos, cold gas around primary galaxies may behave in a different way from what we find here, for those galaxies are more strongly affected by the halo (Catinella et al. 2014). Limited by primary beam effects, we are also unable to investigate how far away from the primary galaxies the conformity phenomenon extends. Limited by the small sample size, we are unable to statistically measure the total HI mass in all the satellite galaxies. Because the accumulative signal ($M_{\text{HI,cand}}$) we obtain is only $\sim 3 \sigma$ above 0, we are unable to calculate spatial gradients, to quantify spatial distribution, or to estimate inflow rate. It also remains unclear how the accreting gas arrives at the HI-excess galaxies, and how much of the HI mass in candidates is not locked into optical galaxies (i.e. in the form of clumps in the more diffuse regions in and between cosmic filaments, or in dark galaxies).

We note that the emphasis of this paper is the exploration of a new technique. We demonstrate the promising potential to investigate HI properties in the radio synthesis cubes below 5-6 σ , which is generally considered as a threshold for detection reliability. We have tried to control the systematics as best as possible and reach the tantalising result that we may have detected evidence for the presence of excess HI in the intergalactic medium around HI rich galaxies. We look forward to applying the technique and analysis presented in this paper to a much larger, more uniform and complete dataset, especially from the ASKAP HI All-Sky Survey, known as WALLABY, and the proposed WSRT Northern Sky HI Survey (WNSHS), both described in Koribalski (2012).

ACKNOWLEDGEMENTS

We thank the anonymous referee for constructive comments. We gratefully thank T. Oosterloo, V. Kilborn, B. Sault, L. Staveley-Smith and S. Huang for useful discussions. J.M. van der Hulst acknowledges support from the European Research Council under the European Union’s Seventh Framework Programme (FP/2007-2013) / ERC Grant Agreement nr. 291531. J. Fu acknowledges the support from the National Science Foundation of China No. 11173044 and the Shanghai Committee of Science and Technology grant No. 12ZR1452700. T. Xiao acknowledges the support from NSFC under Grant No. 11203056.

GALEX (Galaxy Evolution Explorer) is a NASA Small Explorer, launched in April 2003, developed in cooperation with the Centre National d’Études Spatiales of France and the Korean Ministry of Science and Technology.

Funding for the SDSS and SDSS-II has been provided by the Alfred P. Sloan Foundation, the Participating Institutions, the National Science Foundation, the U.S. Department of Energy, the National Aeronautics and Space Administration, the Japanese Monbukagakusho, the Max Planck Society, and the Higher Education Funding Council for England. The SDSS Web Site is <http://www.sdss.org/>.

This publication makes use of data products from the Wide-field Infrared Survey Explorer, which is a joint project of the University of California, Los Angeles, and the Jet Propulsion Laboratory/California Institute of Technology, funded by the National Aeronautics and Space Administration.

REFERENCES

- Agertz O., Teyssier R., Moore B., 2009, MNRAS, 397, L64
 Abazajian K. N., et al., 2009, ApJS, 182, 543
 Becker R. H., White R. L., Helfand D. J., 1995, ApJ, 450, 559
 Binney J., 1977, ApJ, 215, 492
 Brooks A. M., Governato F., Quinn T., Brook C. B., Wadsley J., 2009, ApJ, 694, 396
 Catinella B., et al., 2013, MNRAS, 436, 34
 Catinella B., et al., 2010, MNRAS, 403, 683
 Condon J. J., Cotton W. D., Greisen E. W., Yin Q. F., Perley R. A., Taylor G. B., Broderick J. J., 1998, AJ, 115, 1693
 Conselice C. J., Mortlock A., Bluck A. F. L., Grützbauch R., Duncan K., 2013, MNRAS, 430, 1051
 de Blok W. J. G., et al., 2014, A&A, 569, AA68
 Dekel A., Birnboim Y., 2006, MNRAS, 368, 2
 Di Teodoro E. M., Fraternali F., 2014, A&A, 567, AA68
 Elmegreen B. G., Struck C., Hunter D. A., 2014, ApJ, 796, 110
 Fabello S., Catinella B., Giovanelli R., Kauffmann G., Haynes M. P., Heckman T. M., Schiminovich D., 2011, MNRAS, 411, 993
 Fraternali F., Marasco A., Marinacci F., Binney J., 2013, ApJ, 764, LL21
 Genel S., Bouché N., Naab T., Sternberg A., Genzel R., 2010, ApJ, 719, 229
 Gialalisco M., et al., 2011, ApJ, 743, 95
 Giovanelli R., et al., 2005, AJ, 130, 2598
 Guo Q., White S., Li C., Boylan-Kolchin M., 2010, MNRAS, 404, 1111
 Guo Q., Tempel E., Libeskind N. I., 2014, arXiv, arXiv:1403.5563
 Haynes M. P., 2007, NCimB, 122, 1109
 Heald G., et al., 2011, A&A, 526, AA118
 Heavens A., Panter B., Jimenez R., Dunlop J., 2004, Natur, 428, 625
 Hopkins A. M., McClure-Griffiths N. M., Gaensler B. M., 2008, ApJ, 682, L13
 Huang M.-L., Kauffmann G., Chen Y.-M., Moran S. M., Heckman T. M., Davé R., Johansson J., 2013, MNRAS, 431, 2622
 Huang S., et al., 2014, ApJ, 793, 40
 Kacprzak G. G., Churchill C. W., Nielsen N. M., 2012, ApJ, 760, LL7
 Kauffmann G., 1996, MNRAS, 281, 475
 Kauffmann G., Heckman T. M., De Lucia G., Brinchmann J., Charlot S., Tremonti C., White S. D. M., Brinkmann J., 2006, MNRAS, 367, 1394
 Kauffmann G., Li C., Heckman T. M., 2010, MNRAS, 409, 491
 Kauffmann G., Li C., Zhang W., Weinmann S., 2013, MNRAS, 430, 1447
 Kauffmann G., 2015, MNRAS, 450, 618
 Kennicutt R. C., Jr., 1983, ApJ, 272, 54
 Kereš D., Hernquist L., 2009, ApJ, 700, L1
 Kereš D., Katz N., Davé R., Fardal M., Weinberg D. H., 2009, MNRAS, 396, 2332
 Kereš D., Katz N., Fardal M., Davé R., Weinberg D. H., 2009, MNRAS, 395, 160
 Kereš D., Katz N., Weinberg D. H., Davé R., 2005, MNRAS, 363, 2
 Kitzbichler M. G., White S. D. M., 2008, MNRAS, 391, 1489
 Koribalski B. S., 2012, PASA, 29, 359
 Koribalski B. S., et al., 2004, AJ, 128, 16
 Larson R. B., 1972, Natur, 236, 21
 Lehner N., et al., 2013, ApJ, 770, 138
 Lemonias J. J., Schiminovich D., Catinella B., Heckman T. M., Moran S. M., 2014, ApJ, 790, 27
 Mannucci F., Cresci G., Maiolino R., Marconi A., Gnerucci A., 2010, MNRAS, 408, 2115
 Martin D. C., et al., 2005, ApJ, 619, L1
 McGaugh, S. S., Schombert, J. M., Bothun, G. D., & de Blok, W. J. G. 2000, ApJL, 533, L99
 Moran S. M., et al., 2012, ApJ, 745, 66
 Murray S. D., Lin D. N. C., 2004, ApJ, 615, 586
 Oosterloo T., Fraternali F., Sancisi R., 2007, AJ, 134, 1019
 Pichon C., Pogosyan D., Kimm T., Slyz A., Devriendt J., Dubois Y., 2011, MNRAS, 418, 2493
 Powell L. C., Slyz A., Devriendt J., 2011, MNRAS, 414, 3671
 Putman M. E., et al., 2002, AJ, 123, 873
 Putman, M. E., Peek, J. E. G., & Jounge, M. R. 2012, ARA&A, 50, 491
 Rauch M., Becker G. D., Haehnelt M. G., Gauthier J.-R., Ravindranath S., Sargent W. L. W., 2011, MNRAS, 418, 1115
 Richter P., 2012, ApJ, 750, 165
 Rees M. J., Ostriker J. P., 1977, MNRAS, 179, 541
 Sancisi R., Fraternali F., Oosterloo T., van der Hulst T., 2008, A&ARv, 15, 189
 Schönrich R., Binney J., 2009, MNRAS, 399, 1145
 Schaye J., et al., 2010, MNRAS, 402, 1536
 Serra P., et al., 2015, MNRAS, 448, 1922
 Serra P., et al., 2012, MNRAS, 422, 1835
 Shostak G. S., Skillman E. D., 1989, A&A, 214, 33
 Shull J. M., Jones J. R., Danforth C. W., Collins J. A., 2009, ApJ, 699, 754
 Silk J., 1977, ApJ, 211, 638
 Spitoni E., Matteucci F., Marcon-Uchida M. M., 2013, A&A, 551, AA123
 van de Voort F., Schaye J., 2012, MNRAS, 423, 2991
 Wang E., Wang J., Kauffmann G., Józsa G. I. G., Li C., 2015, MNRAS, 449, 2010
 Wang J., et al., 2014, MNRAS, 441, 2159
 Wang J., et al., 2013, MNRAS, 433, 270
 Wang J., et al., 2011, MNRAS, 412, 1081
 Wang W., White S. D. M., 2012, MNRAS, 424, 2574
 Weinmann S. M., van den Bosch F. C., Yang X., Mo H. J., 2006, MNRAS, 366, 2
 White S. D. M., Rees M. J., 1978, MNRAS, 183, 341
 Wright E. L., et al., 2010, AJ, 140, 1868
 Yates R. M., Kauffmann G., Guo Q., 2012, MNRAS, 422, 215
 Zhang H.-X., Hunter D. A., Elmegreen B. G., Gao Y., Schrubba A., 2012, AJ, 143, 47
 Zhang W., Li C., Kauffmann G., Zou H., Catinella B., Shen S., Guo Q., Chang R., 2009, MNRAS, 397, 1243
 Zwaan M. A., 2001, MNRAS, 325, 1142
 Zwaan M. A., Briggs F. H., 2000, ApJ, 530, L61

APPENDIX A: $M_{\text{HI,cand}}$ ON THE LOW AND HIGH V_{SYS} SIDES OF THE PRIMARY GALAXIES

In the main part of this paper, we report the detection of HI mass ($M_{\text{HI,cand}}$) by adding the candidates outside the galaxies detected in HI cubes (Sect. 3.3). We find $M_{\text{HI,cand}}$ to be higher around galaxies with high HI excess. We have performed tests to show that $M_{\text{HI,cand}}$ is unlikely to be from CLEANing or continuum subtraction residual artefacts (Sect. 3.4). However, as shown in the top-left panel of Figure A1, there is a small gradient in $M_{\text{HI,cand}}$ between the blue and red shifted sides of the HI cube around the primary galaxies. Consequently, part of the difference in $M_{\text{HI,cand}}$ found between sub-samples defined by properties of primary galaxies may be related to this gradient. Indeed, the gradient is slightly stronger for the cubes with low $\Delta_{4p}f_{\text{HI}}$ primary galaxies than the cubes with high $\Delta_{4p}f_{\text{HI}}$ primary galaxies (the second and third panels in the top row of Figure A1); and the difference of $M_{\text{HI,cand}}$ around primary galaxies with

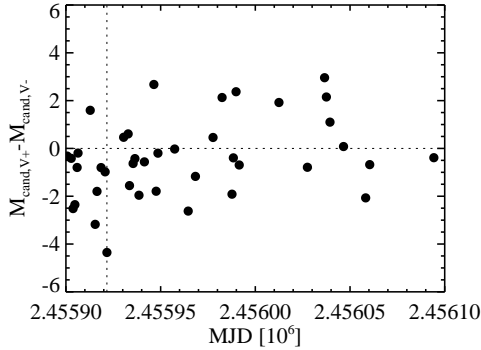


Figure A2. Relation between $M_{\text{HI,cand}}$ gradients and Modified Julian Date (MJD). The vertical dotted line marks the division of the year 2011 and 2012. The horizontal dotted line marks the position of 0.

low and high $\Delta_{4p}f_{\text{HI}}$ is less significant for the low V_{sys} side of the cubes than for the high V_{sys} side of the cubes.

From inspection of the position of candidates in HI cubes, we find that this gradient is not clearly associated with any failures of continuum subtraction, CLEANing or RFI pattern removal. We do not find such gradients in the test with Stokes Q cubes (Sect 3.4). However, we find this gradient is weakly correlated with the date of observation (Figure A2) with a Pearson correlation coefficient of 0.3, mostly driven by the data points for the year 2011, where the distribution of gradients is strongly biased toward negative values. If we exclude the 12 data cubes observed in 2011, the gradients of $M_{\text{HI,cand}}$ is much weaker for the whole sample, and for the primary galaxies with low and high $\Delta_{4p}f_{\text{HI}}$ as well (the first 3 columns in the bottom row of Figure A1). Meanwhile, the difference in $M_{\text{HI,cand}}$ between the two subsamples with low and high $\Delta_{4p}f_{\text{HI}}$ becomes more significant for the low V_{sys} side of the cubes, and is similar for the high V_{sys} side of the cubes (the fourth and fifth columns in the bottom row of Figure A1).

Hence we argue that while the cause for the gradient of $M_{\text{HI,cand}}$ is not found, the effect is not likely to significantly affect our main results, Because it is unclear whether the gradient effect is an artefact or a statistic coincidence, we still use the full sample of 40 data cubes for analysis in the paper. Nevertheless, we warn the readers of this uncertainty in our experiment and intend to investigate it with larger samples in the future.

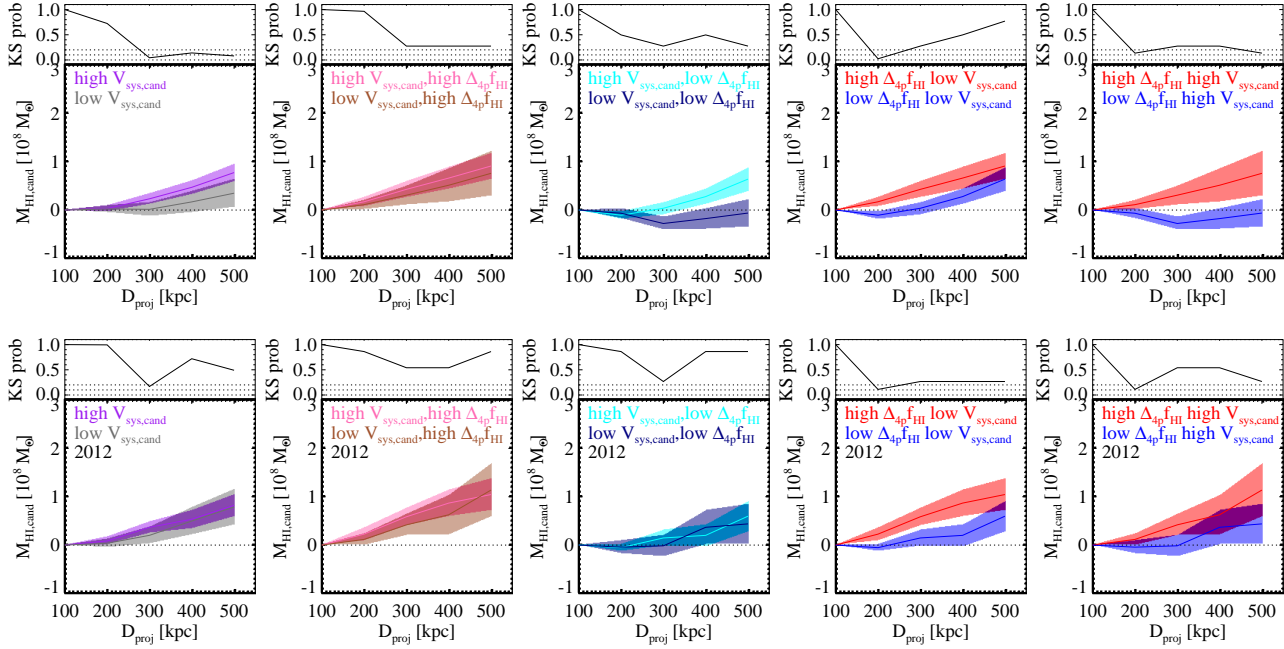


Figure A1. Similar to Figure 10. The candidates are grouped according to their systematic velocity with respect to the primary galaxies, and the $\Delta_{4p} f_{\text{HI}}$ of the primary galaxies in the cubes. The colors of the shades are for the sub-samples denoted in each panel. The top row is for the whole sample of 40 cubes and the bottom row is for the 28 cubes observed in the year 2012.